JACS
JOURNAL OF THE AMERICAN CHEMICAL SOCIETY
pubs.acs.org/JACS
Article

Tunable Band Gaps in MUV-10(M): A Family of Photoredox-Active MOFs with Earth-Abundant Open Metal Sites

Kevin Fabrizio, Konstantinos A. Lazarou, Lillian I. Payne, Liam P. Twight, Stephen Golledge, Christopher H. Hendon,* and Carl K. Brozek*

Cite This: J. Am. Chem. Soc. 2021, 143, 12609−12621
Read Online
ACCESS | Metrics & More | Article Recommendations | Supporting Information

ABSTRACT: Titanium-based metal−organic frameworks (Ti-MOFs) have attracted intense research attention because they can store charges in the form of Ti^{3+} and they serve as photosensitizers to cocatalysts through heterogeneous photoredox reactions at the MOF−liquid interface. Both the charge storage and charge transfer depend on the redox potentials of the MOF and the molecular substrate, but the factors controlling these energetic aspects are not well understood. Additionally, photocatalysis involving Ti-MOFs relies on cocatalysts rather than the intrinsic Ti reactivity, in part because Ti-MOFs with open metal sites are rare. Here, we report that the class of Ti-MOFs known as MUV-10 can be synthetically modified to include a range of redox-inactive ions with flexible coordination environments that control the energies of the photoactive orbitals. Lewis acidic cations installed in the MOF cluster (Cd^{2+}, Sr^{2+}, and Ba^{2+}) or introduced to the pores (H^+, Li^+, Na^+, K^+) tune the electronic structure and band gaps of the MOFs. Through the use of optical redox indicators, we report the first direct measurement of the Fermi levels (redox potentials) of photoexcited MOFs *in situ*. Taken together, these results explain the ability of Ti-MOFs to store charges and provide design principles for achieving heterogeneous photoredox chemistry with electrostatic control.

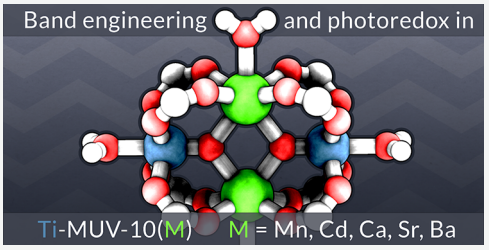

INTRODUCTION

The frontier orbital energies of photocatalysts and molecular substrates dictate key aspects of photoredox reactions, ranging from the thermodynamic driving forces of charge transfer to the wavelengths necessary for photoexcitation.[1−4] Although solid-state materials benefit from greater stability in comparison to homogeneous systems, defining the energetic positions of relevant orbitals, such as the band-edge potentials, is often complicated by compositional defects that dominate the electronic structures.[5,6] Studying site-isolated metal centers in crystalline solids has therefore become an important strategy for investigating interfacial reactivity with molecular control. Whereas the active sites of conventional heterogeneous catalysts can be ill-defined, crystallographic metal centers in metal−organic frameworks (MOFs) combine the atomic precision of molecules with the convenience of solids. In place of typical organic linkers that bridge metal cluster "nodes" in MOFs, such as 1,4-benzenedicarboxylate, "metalloligands" offer an effective approach for installing precise catalytic species. Metalloligands are constructed by functionalizing well-studied homogeneous catalysts with carboxylates or other binding groups to repurpose them as MOF linkers.[7−9] Although they boast improved stabilities, metalloligands exhibit reactivity patterns that still resemble the chemistry of the homogeneous analogues. When they are viewed as discrete coordination complexes, the metal nodes of MOFs, on the other hand, often exist without molecular precedent,[10] thereby enabling unusual small-molecule reactivity,[11] the stabilization of reactive intermediates,[12] and impressive catalytic performance.[13,14] For example, the family of M-MFU-4*l* (M = Ti, V, Cr, Ni, Zn) materials has achieved ethylene oligomerization and polymerization activities superior to those of other homogeneous or heterogeneous catalysts.[13,15−18] MOF metal nodes therefore offer a unique platform for studying interfacial heterogeneous reactivity, whether for uncovering fundamental parameters difficult to pinpoint in less precise heterogeneous systems, e.g., TiO_2, or to discover entirely new chemical transformations. Whereas most reports of catalysis at MOF metal nodes have focused on thermochemical and electrochemical reactions,[19−21] investigations into their photochemical reactivity typically involve cocatalysts. In these systems, photoexcited charges migrate from the MOF clusters to metalloligands, or to impregnated nanoparticles and molecular catalysts, for subsequent reactivity.[22−31] By comparison, the intrinsic photoredox chemistry of MOF nodes remains underexplored.[32−38]

Received: May 9, 2021
Published: August 9, 2021

Downloaded via UNIV OF OREGON on August 18, 2021 at 14:53:51 (UTC).
See https://pubs.acs.org/sharingguidelines for options on how to legitimately share published articles.

© 2021 American Chemical Society

https://doi.org/10.1021/jacs.1c04808
J. Am. Chem. Soc. 2021, 143, 12609−12621

Titanium-based MOFs (Ti-MOFs) offer useful platforms for studying heterogeneous photoredox chemistry. Because the low-lying empty d orbitals of titanium dominate the conduction bands, the lowest-energy optical absorption features can be understood as linker to titanium charge transfer bands.[39] Synthetic manipulation of either the metal or the linker consequently leads to predictable changes to the band gap. For example, the amino-functionalized version of the material known as MIL-125-NH_2 ($Ti_8O_8(OH)_4$(2-amino-terephthalate)$_6$) displays a band gap of 2.6 eV in comparison to the unfunctionalized variant, with a gap of 3.6 eV, resulting from the destabilization of the valence band, composed of linker-based orbitals upon amino functionalization.[40,41] Interestingly, many titanium MOFs are capable of storing charges upon photoexcitation in the presence of sacrificial reductants. For example, irradiating MUV-10(M) ($Ti_3M_3(\mu_3\text{-}O)_2$(1,3,5-benzenetricarboxylate)$_4(H_2O)_6$, M = Ca, Mn) with UV−visible light and excess ethanol leads to the promotion of carboxylate-based electrons to empty titanium orbitals, with the resulting orbital holes quenched by oxidation of ethanol to furnish acetaldehyde and protons (Figure 1). In the absence of

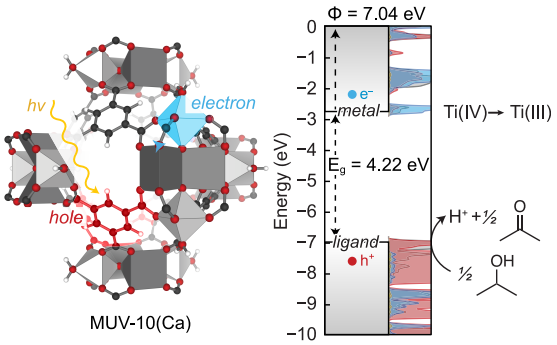

Figure 1. Molecular and band-diagram representations of the photodoping process in MUV-10(Ca). Partial density of states contributions from Ti, O, and C are denoted in blue, red, and black, respectively.

air, such photochemical electronic doping (photodoping) leads to generation of indefinitely stable Ti^{3+} centers that are charge-balanced by H^+.[39] In other words, the H^+−e^- pairs become stabilized at the MOF clusters rather than combine to form H_2. Similar attempts to photodope titanium MOFs featuring single Ti ions rather than multinuclear clusters does not lead to isolation of Ti^{3+}, however. To explain the unique ability of cluster-based Ti-MOFs to generate Ti^{3+} through photodoping, the Martí-Gastaldo group has proposed that clusters tend to produce photoexcited states where the electron localizes on the Ti atoms and the holes center on the linkers.[42] The spatial separation of excited-state charges therefore disfavors rapid electron−hole recombination, allowing ethanol to quench the linker-based hole and trap the Ti^{3+} state. The clusters in these materials typically contain inorganic oxos that bridge titanium centers. In support of the Martí-Gastaldo hypothesis, we propose that bridging oxos prevent H_2 generation by serving as proton acceptors, thereby lowering the electrochemical potential of the H^+−e^- pair. In a similar vein, the Mayer group has justified the charge storage capacity of titanium cluster MOFs in terms of cation−oxo electrostatic pairing stabilization.[43,44] Although MIL-125 nodes contain eight titanium centers, steady-state photoirradiation does not lead to quantitative reduction of all metal ions to Ti^{3+}, as evidenced by electron paramagnetic spectroscopy (EPR). Treatment of MIL-125 particles with sodium-based reductants, however, increases the average number of reduced metal ions per MIL-125 cluster, suggesting a strong cation dependence and ion-pairing effect of charge storage in titanium MOFs.[43] The photoredox chemistry of MOFs, therefore, depends strongly on the chemical factors that control the electrochemical potentials of the resulting photoexcited charges. We therefore seek Ti-MOFs with open metal sites (OMSs) and synthetic tunability for investigating the chemical factors that control photoredox activity.

In designing systems for studying heterogeneous photoredox chemistry, the oxygen-evolving complex (OEC) of Photosystem II (Figure 2) provides a useful example because the

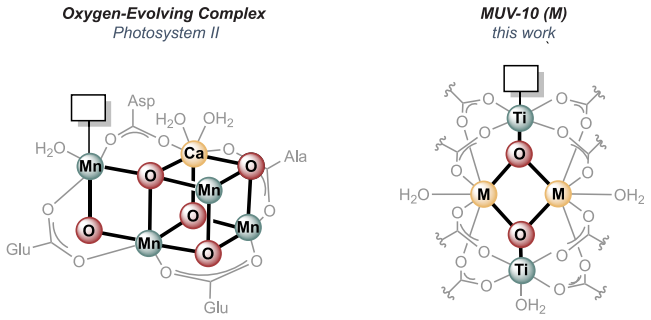

Figure 2. Comparison of the oxygen-evolving complex of Photosystem II and the heterometallic cluster of MUV-10(M). Redox-active metal sites are noted in blue, bridging oxygens in red, redox-inactive metal sites in yellow, and open metal sites as boxes.

Mn_4O_5Ca cluster accomplishes one of the most important examples of photoredox catalysis by harnessing a carboxylate ligand field in a manner akin to typical MOF structures.[45−48] The OEC possesses several design principles for photoactive MOFs: in addition to being comprised of Earth-abundant metal ions, the redox-active Mn^{2+} bears an OMS and a redox-inactive (i.e., redox potential inaccessible under relevant conditions) Ca^{2+} ion influences the energetics of the OEC. Indeed, replacing Ca^{2+} with other alkaline-earth or transition metals leads to systematic shifts in the redox potentials of the native and biomimetic complexes and in the redox chemistry of polyoxometalates.[49−52] We hypothesize that Ti-MOFs containing redox-inactive metal ions would offer a convenient platform for photoredox chemistry with tunable electrochemical properties.

Here, we report that the Ti-MOF known as MUV-10(M)[53] can be expanded into an isostructural family of materials with clusters that incorporate a range of redox-inactive metal ions and Ti centers that support OMSs. Measurement of band gap (HOMO−LUMO) energies reveals that, while the identity of the redox-inactive ions electrostatically shifts the Ti-based orbital energies, their dominant effect is to introduce structural flexibility that strongly affects the optical absorption profiles, especially in the presence of solvent. A similar effect is observed with the introduction of redox-inactive ions to the MOF pores, further illustrating their energetic influence on the orbital energies of photoredox materials. Importantly, the interpretation of these band gap energies required a reevaluation of the applicability of Tauc analysis, which will guide the future analysis of MOFs and other materials in general. Finally, the Fermi levels (electrochemical potentials) of photodoped MUV-10 were approximated using a contact-

https://doi.org/10.1021/jacs.1c04808
J. Am. Chem. Soc. 2021, 143, 12609−12621

less optical redox indicator method, providing evidence of heterogeneous photoredox reactivity and a thermodynamic justification for the charge-storage properties of Ti-MOFs.

EXPERIMENTAL SECTION

Materials and Equipment. All manipulations were performed under an atmosphere of nitrogen in an LC Technology glovebox or by using standard Schlenk techniques. All reagents were purchased from commercial sources and used without further purification. Solvents were purified using a LC Technologies SP-1 solvent purification system. Powder X-ray diffraction (PXRD) patterns were recorded by dispersing activated dry samples on zero-background Si plates using a Bruker D2 Phaser, in the range of 3−35° 2θ using a copper Kα radiation source. N_2 gas sorption isotherms were collected on a Micromeritics ASAP 2020 Plus instrument. X-ray fluorescence data were collected using a Rigaku ZSX Primus II wavelength dispersive X-ray fluorescence spectrometer with a rhodium X-ray source. IR spectra were collected on a Bruker Alpha II spectrometer with an ATR attachment in a nitrogen-filled glovebox and a Nicolet 6700 FT-IR spectrometer with an ATR attachment in open air. UV−vis measurements were performed using a PerkinElmer Lambda 1050 spectrophotometer with a Peltier-cooled InGaAs and PbS detector. MUV-10(M) samples were diluted with $BaSO_4$ as a reference, loaded into a Harrick high-temperature environmental chamber, and attached to a Harrick praying mantis accessory to perform DRUV−vis measurements. The chamber was allowed to equilibrate at a set temperature from 25 to 350 °C for 30 min under dynamic vacuum before each measurement was taken at static vacuum.

Preparation of MUV-10(Ca,Mn). MUV-10(Ca) and MUV-10(Mn) were synthesized according to a literature method.[53] Briefly, a solvothermal reaction of calcium chloride dihydrate (0.0176 g, 0.12 mmol) or manganese(II) chloride tetrahyrate (0.0238 g, 0.12 mmol), titanium(IV) isopropoxide (36 μL, 0.12 mmol), and trimesic acid (0.125 g, 0.595 mmol) in DMF (12 mL), using glacial acetic acid (3.5 mL) as a modulator for crystal growth, was conducted at 120 °C for 48 h in a 50 mL Pyrex Schott bottle.

Preparation of MUV-10(Ba,Sr,Cd). Following a procedure adapted from Castells-Gil et al.,[53] trimesic acid (0.125 g, 0.60 mmol) and barium chloride dihydrate (0.044 g, 0.18 mmol), strontium chloride hexahydrate (0.048 g, 0.18 mmol), or cadmium chloride hemi(pentahydrate) (0.041 g, 0.18 mmol) were placed in a 50 mL Schott bottle and dissolved in dry DMF (12 mL). The solution was then transferred to a benchtop N_2 glovebox, where glacial acetic acid (3.5 mL for Cd/Sr and 5.0 mL for Ba) and titanium(IV) isopropoxide (36 μL, 0.12 mmol) were added, and the bottle was resealed. Then, the solution was heated in a fixed-temperature oven at 120 °C for 48 h. The resulting white powder was centrifuged, washed three times sequentially with 20 mL of clean DMF and methanol, and then dried under dynamic vacuum overnight at room temperature.

Fermi Level Estimation by Optical Redox Indicator. In an N_2 glovebox, decamethylferrocene ($FeCp^*_2$) was weighed into a Schlenk flask and dissolved in ca. 5 mL of hexanes. In air, benzoquinone was dissolved in ca. 5 mL of ethyl ether, and HBF_4 was added. The $FeCp^*_2$ and benzoquinone solutions were combined by cannula transfer, creating a cloudy dark green mixture. This solution was stirred for 1 h and let stand for 30 min, yielding a green precipitate. The flask was transferred to a benchtop N_2 glovebox, where the contents were vacuum filtered and the residue washed with dry hexanes (~40 mL). Once it was transferred into a standard N_2 glovebox, the powder was dissolved in dry MeCN. The concentration of the solution was tested via UV−vis by way of a dilution of 300 μL in 3 mL of MeCN in an air-free quartz cuvette with a path length of 1 cm, and the concentration was determined to be 4.06 mM by the 30 min irradiation absorbance value at 778 nm for an absorptivity coefficient of 488 L mol^{-1} cm^{-1}, according to prior studies of the decamethylferrocene/decamethylferrocenium ($[FeCp^*_2]/[FeCp^*_2]^+$) redox couple.[54] Similarly to the previous experiment, 3 mg of MUV-10(Ca) was added to 3 mL of stock $[FeCp^*_2]^+$ in MeCN and 300 μL of dry ethanol. The cuvette was irradiated with a mercury arc lamp, and the UV−vis spectra were recorded after allowing the powder to settle. After 1290 min of irradiation (21.5 h) the vibrant green solution had turned yellow, indicating the complex's conversion to $FeCp^*_2$.

Soaking MUV-10(Ca) in Nitrate Salts. The effect of H^+ on MUV-10(M) was tested by soaking 1 mg of MUV-10(Ca) in 2 mL of 10^{-3} M HNO_3 overnight (>16 h) and then measuring the diffuse reflectance spectrum. Similarly, the effect of different cations was examined by preparing suspensions consisting of 2 mL aqueous solutions of $LiNO_3$, $NaNO_3$, and KNO_3, respectively, together with 1 mg of MUV-10(Ca) such that the ratio of cation to Ti in the MOF would be 5:1. After every soaking experiment, a powder diffraction pattern was collected to ensure that the crystal lattice remained intact (Figure S23).

Computational Methods. Density functional theory (DFT) calculations were performed to identify the density of states (DOS) and band gap energy (E_g) of MUV-10 (M) derivatives, in addition to different hydration states and cation localization on the MOF cluster.

All MOF structures were geometrically equilibrated with the GGA functional PBEsol[55] in VASP[56−58] and a 500 eV plane-wave cutoff basis set. A Γ-only k grid was converged to ionic and electronic criteria of 0.005 and 1×10^{-6} eV, respectively. Then, using the range separated hybrid GGA approach HSEsol06[59] (PBEsol + 25% HF), the electronic band gap was computed using the same convergence criteria as above. This approximation was determined to be suitable, as the PBEsol electronic band structure (Figure S40) revealed that MUV-10(Ca) has extremely flat bands, indicating a direct band gap, and localized electronic states. Thus, Γ-only is suitable to assess the band gap.

In the transmetalated structures, all of the Ca atoms in the unit cell were exchanged for the respective metal before a full optimization. For the hydrogen-functionalized structures, one inorganic oxo in the unit cell was functionalized with a hydrogen atom. The same procedure was followed for the proton functionalized structures, with one electron removed from the unit cell to constitute the addition of a proton. Manganese and cadmium structures were converged with H_2O coordinated solely to titanium at the nodes. The manganese-substituted parent scaffold was found to have lower energy in the antiferromagnetic configuration, and so the electronic structures of all manganese-substituted derivatives were calculated in the antiferromagnetic state. We present a comparison of the manganese structure in Figure S33.

Finally, both hydrogen-functionalized and parent bulk structures were aligned to the vacuum level using a previously reported method.[60] In brief, we probe the internal electrostatic potential at the center of the pore, using the method depicted in Figure S35.

RESULTS AND ANALYSIS

Preparation of the MUV-10(M) Isostructural Series. The Ti-MOF known as MUV-10(M), where M = Ca, Mn, was selected as a molecularly defined platform for studying heterogeneous photoredox chemistry. In an idealized disorder-free model, the heterobimetallic clusters of MUV-10(M) consist of two octahedral Ti(IV) centers bridged to two heterometals by inorganic oxos and trimesate carboxylate linkers (Figure 2). The combination of the carboxylate and aqueous ligand environments, the metal−oxo architecture, redox-inactive heterometals, and photoactive Ti ions with OMSs therefore renders MUV-10(M) an ideal candidate for pursuing the design principles of the oxygen-evolving complex (OEC) of PSII. Just as the redox-inactive heterometal tunes the redox chemistry of OEC and molecular inorganic clusters, we sought to prepare analogues of MUV-10(M) with a range of metal ions, on the basis of the hypothesis that they would influence the $Ti^{4+/3+}$ reduction potential through electrostatic interactions. By building a library of MUV-10(M) variants, we

https://doi.org/10.1021/jacs.1c04808
J. Am. Chem. Soc. 2021, 143, 12609−12621

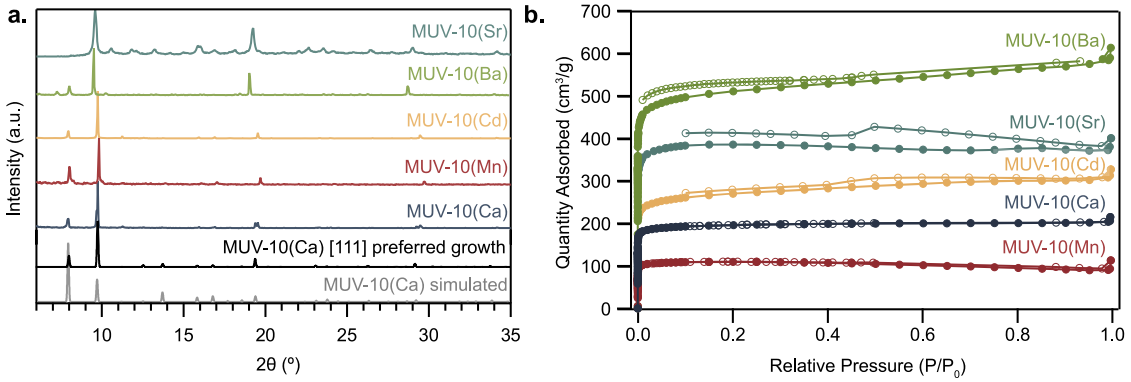

Figure 3. (a) Powder X-ray diffraction patterns of MUV-10(M) (M = Ca^{2+}, Mn^{2+}, Cd^{2+}, Ba^{2+}, Sr^{2+}). Simulated patterns are shown on the basis of isotropic and preferred growth in the [111] direction. (b) N_2 gas sorption measurements of MUV-10(Sr,Ba,Cd) derivatives collected at 77 K. Adsorption curves are denoted by full circles and desorption by open circles. MUV-10(Ca) and MUV-10(Mn) are shown as a comparison to the new derivatives.

planned to investigate the energetic effect of cations on the electronic structure of photoredox materials.

Three new MUV-10(M) derivatives (M = Ba, Sr, Cd) were prepared by a modified solvothermal synthesis. Figure 3a plots the powder X-ray diffraction (PXRD) patterns, confirming retention of the original MUV-10(Ca) structures. Attempts to synthesize MUV-10 solely from Sr^{2+}, Ba^{2+}, or Cd^{2+} precursors yielded amorphous materials. We note that an attempt at postsynthetic cation exchange in MUV-10(M) was recently reported not to yield isostructural products.[61] Although relative peak intensities differ from the calculated geometries as is, simulating preferred growth in the [111] direction shows almost an identical fit, with the [222] and [333] phases growing in intensity as well (Figure S1). Furthermore, a recent report on the applications of MUV-10(Ca) particles note that by simulating the equilibrium shape of the crystal, the (111) planes energetically show preferential formation with minor contributions from the (001) planes.[62] Correspondingly, the (110) and (111) Bragg intensities have differed by varying crystal growth modulator equivalents in nanoparticle syntheses of MUV-10(Ca).[63] While attempts to incorporate Mg^{2+} to complete the series of alkaline-earth metals did not yield a crystalline product, a recent study demonstrated that the inclusion of Mg^{2+} results in a separate MOF isostructural to the MIL-100 family.[64] We suspect that the ionic radius is a critical determinant of isostructural MOF syntheses, given that the ionic radius for Mg^{2+} in a six-coordinate geometry is 0.72 in comparison to Ca^{2+} (1.0), Mn^{2+} (0.83), Ba^{2+} (1.35), Sr^{2+} (1.18), and Cd^{2+} (0.95).[60] Interestingly, computational methods in the seminal report on MUV-10(Ca,Mn) predicted that an MUV-10(Cd) variant would be the least thermodynamically favorable, and yet we demonstrate that it can be prepared following similar procedures. Cd^{2+} was targeted in order to compare the energetic effect of a d^{10} transition-metal ion in comparison to Mn^{2+}, which is d^5, and to expand upon examples of redox-inactive variants beyond alkaline-earth metals. X-ray fluorescence spectra of all powders confirmed that both metal ions are incorporated into the structures (Figures S1−S7). X-ray photoelectron spectroscopy reveals the anticipated metal ion valences and confirms a 1:1 Ti^{4+}:M^{2+} ratio in MUV-10(Sr) and MUV-10(Cd). The results for MUV-10(Ba) suggest an excess of titanium, however. Inductively coupled plasma mass spectrometry (ICP-MS) further corroborates these findings, with the Cd and Sr analogues possessing the anticipated stoichiometry, whereas the Ba material shows excess Ti. The synthesis of MUV-10(Ba) qualitatively produced a gel-like byproduct that could be largely removed with washing. Residual gel in the elemental analysis of this material could contribute to the nonstoichiometric ratio of metal ions. Moreover, attempts to synthesize derivatives with nonstoichiometric equivalents of heterometal (Ba, Sr, Cd) were unsuccessful, which demonstrates the necessary presence of a heterometal.

For further evidence of isostructural MUV-10(M) derivatives, N_2 gas sorption isotherms were measured at 77 K for MUV 10(Ba,Sr,Cd) following activation under vacuum at 130 °C. Figure 3b plots both adsorption and desorption data, revealing the expected type I isotherms and reversibility for all materials. A multipoint Brunauer−Emmett−Teller (BET) analysis yields specific surface areas of 1902.99, 1227.63, and 871.44 m^2/g (2.89×10^6, 1.68×10^6, 1.27×10^6 m^2/mol), for Ba, Sr, and Cd, respectively. The Ba^{2+} and Sr^{2+} variants showed surprisingly high uptake, in qualitative comparison with that of the Cd^{2+} derivative. We hypothesize that the increased surface areas can be attributed to their large ionic radii (1.35 and 1.18 Å, respectively), which may not only expand pore sizes but also create linker vacancies through lattice strain.[65] The increased quantity of defects and disorder (interstitial vacancies in the lattice, M^{2+}, or linker) present in these two derivatives allows for higher N_2 uptake in comparison to that of more pristine derivatives (Ca^{2+}, Cd^{2+}, Mn^{2+}). We further analyzed the powder patterns for experimental unit cell parameters and noted that the larger ionic radii cause unit cell expansions of almost 0.5 Å in comparison to MUV-10(Mn) (Table S1). The correlations between unit cell dimensions and large ionic radii of the heterometal in MUV-10(M) are further represented in the experimental powder patterns, which shift to slightly lower 2θ values, suggesting an increase in unit cell volume. As a final point of comparison, we simulated the solvent-accessible pore space in the geometry-optimized structures (Table S2) and noted that the Ba and Sr analogues have the highest uptake, which complements their higher experimental N_2 gas sorption isotherms.

Generation of Photoactive Open Metal Sites. For insight into the structural stability of the new MUV-10(M) derivatives and for initial evidence that they support OMSs via the removal of water ligands, we performed a thermogravimetric analysis (TGA). All three derivatives (Ba, Sr, Cd) show

https://doi.org/10.1021/jacs.1c04808
J. Am. Chem. Soc. 2021, 143, 12609−12621

thermal stability to 475 °C and significant weight losses below 150 °C: 21.03% for MUV-10(Ba), 24.48% for MUV-10 (Sr), and 13.42% for MUV-10(Cd) (Figure 4). On the basis of the

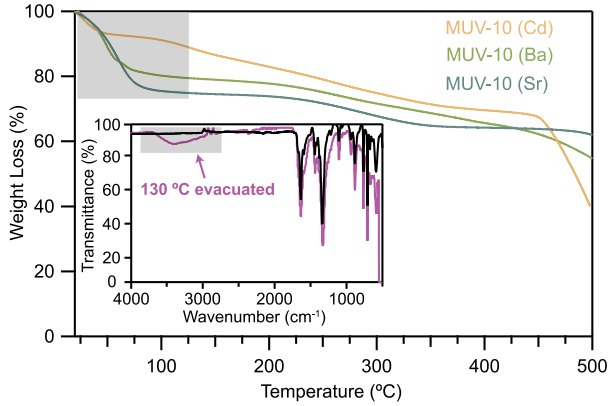

Figure 4. Thermogravimetric analysis for new MUV-10(M) derivatives (M = Cd, Ba, Sr) showing a significant weight loss between 0 and 100 °C after solvent exchange and activation at elevated temperatures. Inset: IR spectra of as-prepared MUV-10(Ca) and activated MUV-10(Ca), suggesting a loss of the −OH stretch in water at 3700−3000 cm^{-1}.

assumption that one water molecule coordinates to each metal in an idealized formula unit of MUV-10(M), we would anticipate a weight loss of 6.65% for MUV-10(Ba), 7.60% for MUV-10(Sr), and 6.97% for MUV-10(Cd) for the complete removal of terminally bound aqua ligands. Because the actual weight losses for all three derivatives are markedly higher than expected, we attribute these weight changes to loss of pendant water molecules, interactions of the alkaline-earth metals with excess water (as evidenced by the difference in experimental weight losses between MUV-10(Ba,Sr)) and MUV-10(Cd)), and residual water/methanol mixtures from the pores. For direct evidence of OMS generation, we compared Fourier transform infrared (FT-IR) spectra of all derivatives before and after treatment with vacuum at 130 °C. Figure 4 compares IR spectra of the as-prepared and evacuated materials, showing the disappearance of the broad peak associated with the −OH stretch of water. Given prior evidence from CO adsorption studies that water can be removed from the Ti sites of MUV-10(Ca),[65,66] these data suggest MUV-10(M) comprises an unusual family of photoactive MOF with OMSs. Given the ability of MUV-10(M) to stabilize Ti^{3+}−H^+ pairs, we envisioned use of these materials for photoredox transfer hydrogenation catalysis, where bond formation to substrates at photoactive OMS will be beneficial.

Electrostatic Control of Band Gap Energies. UV−vis spectra were collected *in situ* of all materials during evacuation and heating to probe changes in the titanium ligand field upon water removal and for evidence that varying the heterometal identities electrostatically tunes the titanium redox potentials. Because the Ti 3d orbitals dominate the composition of Ti-MOF conduction bands, we reasoned that changes to the band gap energies can be interpreted in terms of alterations to the $Ti^{4+/3+}$ redox potential. For example, if a chemical modification causes the conduction band edge to lower in energy and narrow the band gap, then the $Ti^{4+/3+}$ redox potential is therefore stabilized. Figure 5a−e plot UV−vis spectra of MUV-10(Ca,Mn,Cd,Sr,Ba) collected in diffuse-reflectance spectroscopy. The spectra compare the samples analyzed under ambient-pressure N_2 at 25 °C vs dynamic vacuum with heating between 25 and 350 °C. By collecting spectra *in situ*, we were therefore able to monitor the dehydration and creation of OMSs in the MUV-10 family. Plotted in Kubelka−Munk units, all 25 °C spectra exhibit a gradual increase in absorption beginning around 3.0 eV and maximizing near 4.5 eV. When they are heated under dynamic vacuum to 350 °C, however, all samples show a significant increase in absorption at lower energies, beginning at around 2.0 eV. By assigning the peak maximum to an O(2p)−Ti(3d) ligand to metal charge transfer (LMCT) band, dehydration and variation of the heterometal identities were expected to shift the $Ti^{4+/3+}$ redox couples and, hence, peak maxima. The pronounced absorption tails at higher temperatures, however, were unexpected. Rather than simple shifts to band gap energies, we suspected that the low-energy absorption features arise from thermally activated distortions to the Ti ligand sphere, thereby creating transitions between midgap defect orbitals. With this in mind, the defects could be irreversibly formed, such as by water removal, or they could form reversibly, such as by thermally induced dynamic bonding between "tight" and "loose" configurations (Figure 5f), as reported recently.[67]

Figure 6 shows that the absorption tailing across 20−250 °C is reversible, suggesting a thermodynamically controlled equilibrium process rather than an irreversible creation of defects. Consequently, assigning band gap energies and interpreting the electronic structures of MUV-10(M) materials depends on identifying the origin of such low-energy features.

Choosing methods for assigning band gap energies depends on whether low-energy absorption tails arise from the band edges or from midgap orbitals. On one hand, the peak maxima can be taken as the excitation of a valence-band electron to the conduction band. If many overlapping bands contribute to the absorption onset, however, the band gap energy can be determined from the intersection of the energy axis and a linear fit of the absorption edge, known as a Tauc plot analysis. Superficially, the absorption profiles of all derivatives, except MUV-10(Mn), display increased absorption at lower excitation energies, suggesting that dehydration causes a considerable band gap narrowing of nearly 1.0 eV by Tauc analysis in the case of MUV-10(Cd). Increased absorption involves pronounced tailing of the optical bands rather than significant shifts to the band maxima, however. Understanding the origin of such drastic changes to optical absorption requires a precise knowledge of the electronic structures of MUV-10(M) materials.

Figure 7 shows the computed DOS diagrams for MUV-10(Ca) in different states of hydration in comparison to experimental values. The "fully hydrated" structure was constructed with one H_2O bound to each Ti and Ca metal site. The "partially hydrated" structures feature just a single H_2O bound to each titanium atom, and "dehydrated" includes no H_2O ligands. Because, experimentally, the degree of hydration cannot be quantified *in situ*, the empirical band gap value for the "partially hydrated" analogue has not been measured. Upon full dehydration, however, the calculated band gaps narrow by ∼100 meV from 4.22 to 4.11 eV. Inspection of the electronic structures suggests that the frontier orbitals remain largely intact and simply shift toward lower-energy potentials as a result of water removal. To compare these computed band gaps to experimental values, we attempted a Tauc analysis of MUV-10(Ca) at 25 °C, which involved fitting the absorption band tails, yielding a gap of 3.83 eV. The

https://doi.org/10.1021/jacs.1c04808
J. Am. Chem. Soc. 2021, 143, 12609−12621

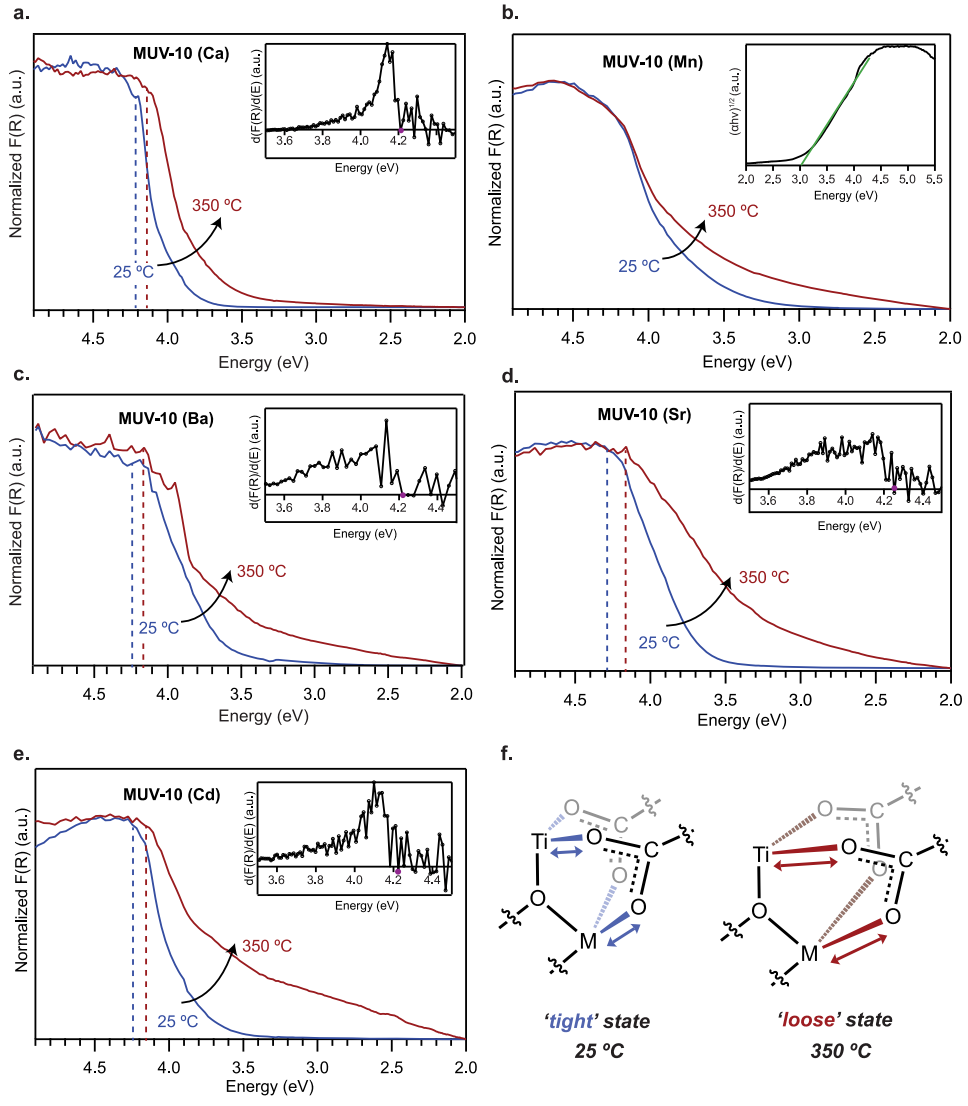

Figure 5. (a–e) Variable-temperature diffuse reflectance UV–vis–NIR spectra for MUV-10(Ca,Mn,Cd,Ba,Sr) to monitor dehydration. Dashed lines indicate band gap energies determined by a derivative analysis (Ca, Ba, Sr, Cd) or a Tauc plot analysis (Mn). Insets show derivative or Tauc plots. (f) Scheme of "tight" and "loose" states of dynamic metal–carboxylate bonding in the MUV-10(M) cluster at high temperatures.

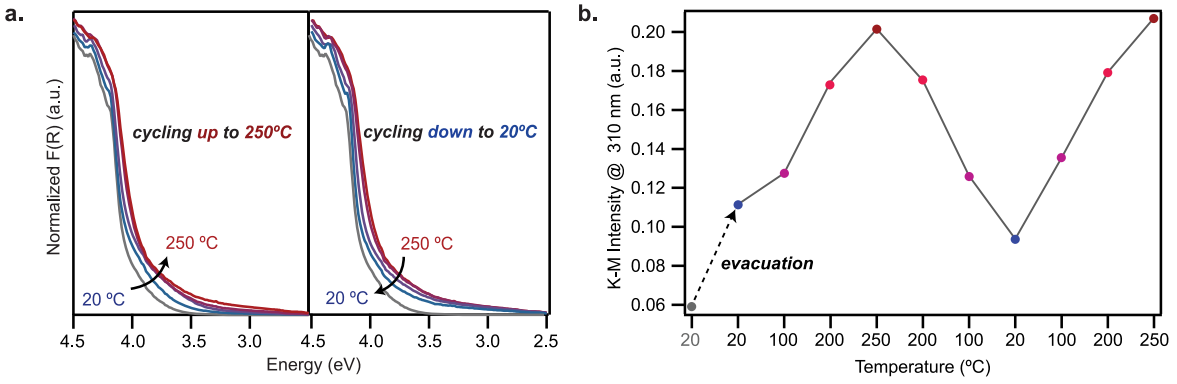

Figure 6. (a) Diffuse reflectance UV–vis data of MUV-10(Ca) collected under dynamic vacuum and cycled between 20 and 250 °C. (b) Kubelka–Munk intensities at 4.0 eV versus temperature.

difference between this value and the computed gap of 4.22 eV was outside the typical margin of error for this level of theory, however. Derivative analysis, on the other hand, produced a band gap of 4.21 eV, which is nearly identical with the computed value. The prominence of absorption tails at higher temperatures therefore cannot be attributed to a well-ordered structural change. We reasoned that the dynamic metal–linker bonding of MUV-10(Ca), as detailed previously,[67] could give

https://doi.org/10.1021/jacs.1c04808
J. Am. Chem. Soc. 2021, 143, 12609–12621

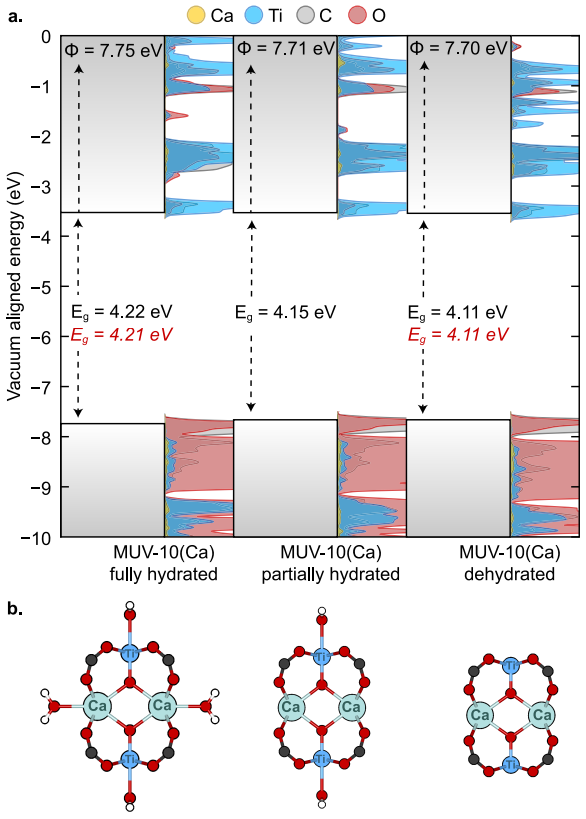

Figure 7. (a) Density functional theory (DFT) density of states (DOS) calculations for "fully hydrated" MUV-10(Ca), "partially hydrated" MUV-10 (Ca), and "dehydrated" MUV-10(Ca). Experimental and computed band gap energies are shown in red and black, respectively. (b) Geometry-optimized structures for three forms of MUV-10(Ca) hydration.

rise to the absorption tail by creating midgap orbitals that arise from disorder around the MOF node. A thermally induced shift of the bonding equilibrium from "tight" to "loose" binding is also consistent with the reversibility evidenced in Figure 6.

To understand the effect of varying heterometals on the electronic structures of MUV-10(M) materials, we computed DOS diagrams of all "fully hydrated" MUV-10(M) derivatives (Figure 8). A comparison of the MUV-10(Ca,Sr,Ba) electronic structures shows a clear electrostatic influence of the alkaline-earth metals, with heavier elements exerting greater stabilization on frontier orbital energies. For example, replacing Ca^{2+} with Ba^{2+} causes the O-based valence band to shift by 50 meV and the Ti-based conduction band to be stabilized by 140 meV.

By a Tauc analysis, a comparison of computed band gap energies did not match the experimental results, except for MUV-10 (Mn). Derivative analysis, however, yielded experimental band gap energies in close agreement with theory (Table 1). These results suggest that the chemical factors

Table 1. Comparison of Experimentally Determined Band Gap Energies for Fully Hydrated MUV-10(M) Using Tauc Analysis and Derivative Analysis versus DFT Calculated Band Gap Energies

	E_g (eV)		
MOF name	Tauc	Derivative	DFT
MUV-10(Ca)	3.83	4.21	4.22
MUV-10(Mn)	3.03	4.34	2.78
MUV-10(Sr)	3.29	4.25	4.17
MUV-10(Ba)	3.29	4.21	4.13
MUV-10(Cd)	3.54	4.18	4.13

contributing to the absorption tail do not arise from simple alterations to the heterometal identities. Instead, the optical band gaps of the MUV-10(Ca,Ba,Sr,Cd) materials are best described as valence to conduction band edge transitions, regardless of the hydration state and presence of midgap orbitals. For example, in the case of MUV-10(Ca) the band gap energy determined by a Tauc analysis is 0.40 eV less than expected, whereas derivative analysis is off within a margin of error (0.01 eV) for this technique. We propose that, whereas most MUV-10 materials exhibit wide band gap transitions

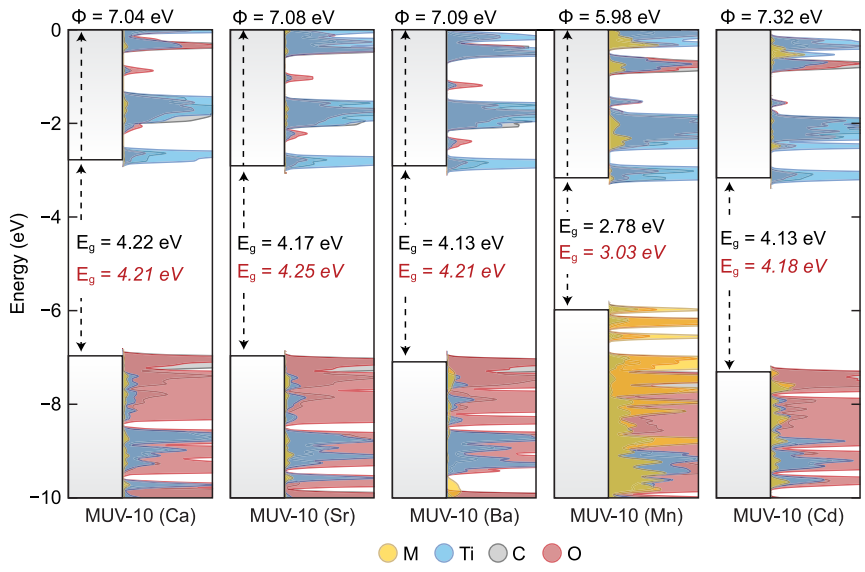

Figure 8. Density functional theory DOS calculations for all hydrated derivatives. Experimentally determined values are shown in red, either by derivative analysis (Ca, Sr, Ba, Cd) or Tauc analysis (Mn).

https://doi.org/10.1021/jacs.1c04808
J. Am. Chem. Soc. 2021, 143, 12609−12621

appropriate for derivative analysis, band gap assignment of MUV-10(Mn) requires a Tauc analysis because the multitude of ligand-field transitions overlap with the O(2p)−Ti(3d) absorption band. Because proton-coupled electron transfer and, more broadly, ion-coupled charge transfer of Ti-MOFs have been described in terms of electrostatic interactions between soluble cations and MOF nodes, we investigated the effect of introducing cations to the MUV-10(Ca) pores. In particular, we were interested in whether the electrostatic influence of cations could explain the high charge capacitance of Ti-MOFs, with recent evidence for H^+ and Na^+ coordination to the oxo bridges of the Ti_8O_8 molecular cluster analogue of MIL-125.[43] Given the electrostatic impact of redox-inactive cations *within* the MUV-10 node, introducing soluble cations *outside* the node offers a means to compare the effect of cation location. After activation at 130 °C under a dynamic vacuum, MUV-10(Ca) was soaked in 0.1-M inorganic nitrate salt solutions ($LiNO_3$, KNO_3, $NaNO_3$) and 10^{-3}-M HNO_3. The stability and phase purity after cation treatment were confirmed by PXRD (Figure S23). Following cation treatment, the optical absorptions of all materials were analyzed at 25 °C via diffuse reflectance UV−vis spectroscopy (Figure 9). Rather than simple shifts to the band maxima, all

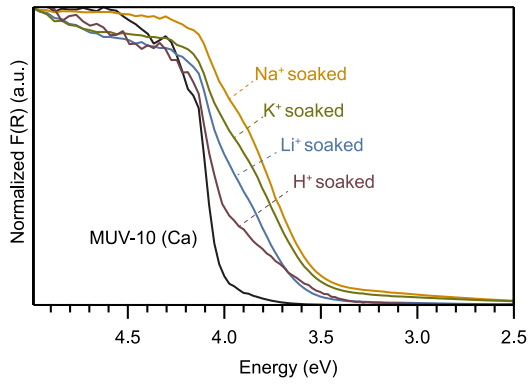

Figure 9. Diffuse reflectance UV−vis−NIR spectra of MUV-10(Ca) soaked with different nitrate salts.

spectra show the emergence of new, lower-energy absorption with the introduction of soluble cations. We hypothesized that the cations bind to the MOF nodes, causing a lowering in symmetry and, hence, the introduction of midgap orbitals that cause low-energy absorption. Due to differences in size, we expect the series of alkali metals to exhibit different binding modes to the MUV-10(Ca) SBU and, hence, different UV−vis spectra. Although inappropriate for the wide-gap MUV-10(Ca) without cations, a Tauc analysis is suitable for analyzing materials with overlapping bands arising from midgap orbitals. In comparison to hydrated MUV-10(Ca) (3.83 eV), a Tauc analysis of all cation-soaked samples indicates considerable narrowing of band gap energies, with H^+-MUV-10(Ca) showing a gap of just 3.22 eV (Table 2). To explore the origin of this cation-induced effect, we computed the DOS for H^+-MUV-10(Ca) modeled by placing H^+ near the nodes and allowing the structure to relax (Figure 10). In comparison with the DOS of hydrated MUV-10(Ca), the DOS of H^+-MUV-10(Ca) shows the valence band destabilizing by 900 meV but the conduction band stabilizing by 740 meV. Additionally, protonation breaks the energetic degeneracy of MUV-10(Ca) orbitals, causing the initially sparse electronic structure to

Table 2. External Cation Incorporation into MUV-10(Ca) Band Gap Energy Comparisons via Tauc Plot Analysis

MOF name	E_g Tauc (eV)
MUV-10(Ca)	3.83
H^+-MUV-10(Ca)	3.22
Li^+-MUV-10(Ca)	3.39
K^+-MUV-10(Ca)	3.20
Na^+-MUV-10(Ca)	3.24

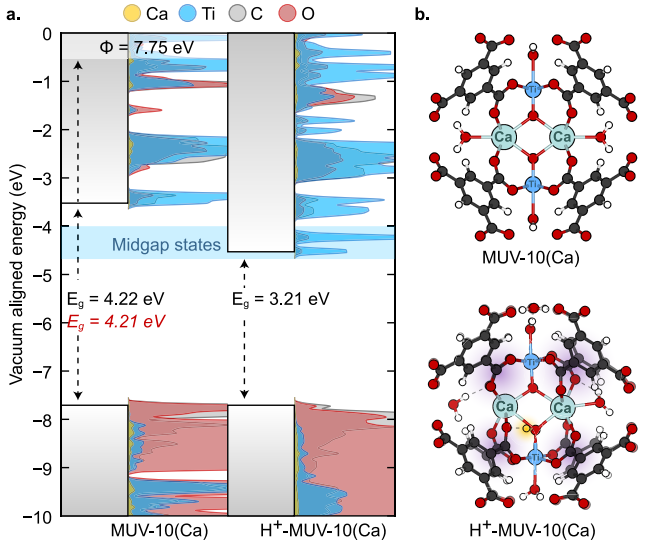

Figure 10. (a) Computed DOS diagrams for hydrated MUV-10(Ca) and H^+-MUV-10(Ca) with midgap states highlighted in light blue. (b) Optimized structures for hydrated MUV-10(Ca) versus H^+-MUV-10(Ca). The adatomic proton is highlighted in yellow.

spread into many inequivalent orbitals, indicating a lowering of symmetry. Indeed, the computed structure of H^+-MUV-(10) shows considerable disorder around the node, caused by H^+ binding to the oxo bridges (Figure 10b).

Measurement of Light-Induced Fermi Levels. Evidence for tunable band gaps and frontier orbital energies of MUV-10(M) provide a basis for understanding the energetics of Ti-MOF photoredox activity. To complement these insights, we therefore sought to measure the redox potentials of MUV-10(M) under photoredox conditions. Inspired by prior reports of colloidal semiconductor nanocrystals,[68−70] we sought to use a soluble optical redox indicator as a contactless probe of the Fermi-level energy (E_F) of MUV-10(M) during photoredox chemistry. This method involves suspending MOFs in solution with a molecule having an electrochemically reversible redox couple that gives rise to distinct sets of optical bands. When the MOF and redox indicator are allowed to equilibrate, changes to the UV−vis spectra of the molecule therefore indicate that the MOF has also experienced changes in its redox state: i.e., E_F. The absolute absorbance of the optical redox indicator in a given redox state can be related through the appropriate extinction coefficient to its solution concentration. For example, if the absorbance of the reduced state of a molecule decreases, then the new, decreased concentration of the reduced species can be determined. Through the Nernst equation, the ratio of the oxidized and reduced forms of the optical redox indicator can be used to derive a solution E_F, which is equivalent to the E_F value of the MOF after equilibration. As a proof-of-concept photoredox reaction, we

https://doi.org/10.1021/jacs.1c04808
J. Am. Chem. Soc. 2021, 143, 12609−12621

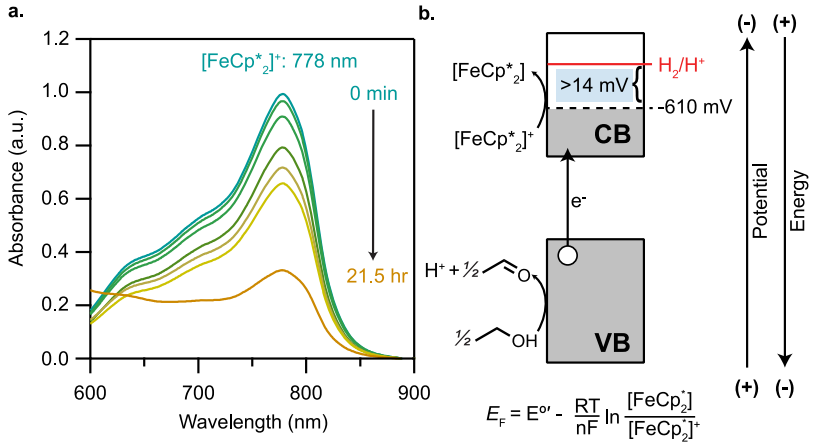

Figure 11. (a) Solution-state UV−vis spectra of photodoping MUV-10(Ca) powder with excess optical redox indicator $[FeCp^*_2]^+$. (b) Band-diagram representation of the photodoping process in MUV-10(Ca).

sought to measure the E_F of MUV-10(M) under photodoping conditions. In brief, the photoredox chemistry would involve the photoexcited MOF oxidizing ethanol, accumulating conduction-band electrons, and exchanging charges with an optical redox indicator (Figure 11b). By monitoring the absorption of the indicator, we would thereby measure the steady-state E_F *in situ*. In an air-free quartz cuvette, MUV-10(Ca) was suspended in 3 mL of dry acetonitrile with excess ethanol and decamethylferrocenium ($[FeCp^*_2]^+$) (1.5:1 $[FeCp^*_2]^+$:Ti^{4+}) as an optical redox indicator. The mixture was irradiated with a broad-band photolysis lamp, and the concentration of $[FeCp^*_2]^+$ and, hence, the $[FeCp^*_2]^+$:$[FeCp^*_2]$ ratio were determined from the absorbance at 778 nm, attributable to an LMCT transition of $[FeCp^*_2]^+$.[54,71,72] Figure 11a shows a gradual decrease in the absorption bands of $[FeCp^*_2]^+$, indicating photoreduction by MUV-10(Ca). After 21.5 h of irradiation, the system reached a steady state, as indicated by no further decrease in absorption bands. Calculating the concentration of $[FeCp^*_2]^+$ suggests that MUV-10(M) reduced 67% of the indicator, giving a steady-state redox potential, i.e., E_F, of −610 mV vs Fc^+/Fc.[71] This redox potential sits 14 mV positive of the electrochemical potential for the hydrogen evolution reaction (HER) in acetonitrile: −624 mV vs Fc^+/Fc at pH 1.[71] In a similar experiment using instead the cobaltocenium/cobaltocene redox couple (−1.33 V vs Fc^+/Fc), no photoreduction was observed, which is consistent with the steady-state E_F of photodoped MUV-10(Ca) being assigned to the milder potential of −610 mV vs Fc^+/Fc.

DISCUSSION

These results indicate that the frontier orbital energies (band-edge potentials) and band gaps of MUV-10(M) can be tuned by redox-inactive cations. Similar effects have been widely reported for a range of molecular and material systems, including biomimetic models of the oxygen-evolving cluster,[49,50] synthetic Fe−oxo complexes,[73,74] polyoxovanadate anions,[51] and semiconductor nanocrystals.[68,69,75−78] In these systems, Lewis acidic ions, e.g., Na^+, Ca^{2+}, and Sc^{3+}, modulate redox potentials by hundreds of millivolts through electrostatic interactions. Whereas harder Lewis acids, such as Sc^{3+}, typically induce greater stabilization, the computational results presented here indicate the opposite trend, where MUV-10(Sr) and MUV-10(Ba) exhibited lower Ti-based orbitals in comparison to MUV-10(Ca). A key caveat to interpreting this result is that optical absorption energies do not involve nuclear rearrangement in the excited state, while redox potentials are affected by the nuclear motion associated with ion pairing.[79] In other words, the stronger influence of harder Lewis acids may be borne out only when they can rearrange to bind more tightly. Instead, we propose that the Ti-based orbitals become stabilized by the larger lattices created by the softer Sr^{2+} and Ba^{2+} ions. The use of framework vs external cations also draws interesting comparisons to the electrostatic effect of redox-inactive cations in degenerately doped semiconductor nanocrystals.[76,80,81] Whereas aliovalent dopants, such as Sn^{4+} in In_2O_3, exert greater stabilization on the potentials of delocalized charges in comparison to surface-bound electrolyte, MOFs lack conventional "bulk" interiors and can be viewed instead entirely as "surface". Consequently, the introduction of soluble cations had a systematic effect on MUV-10(M) band gap energies and electronic structure because every MOF node could be accessed and distorted by the cations. We therefore argue that the electrostatic influence of the electrolyte in the pores of MOFs play an important role in determining MOF properties, in general.

Evidence for cation-induced stabilization of Ti-based orbitals helps explain the ability of Ti-MOFs to photodope and trap Ti^{3+}−H^+ pairs. Because photodoping of Ti-MOFs involves trapping an electron as Ti^{3+} and the liberation of H^+, the e^-−H^+ pair has the potential to recombine as H_2, but energetic aspects of the process ensure that it does not. These results support several hypotheses put forward by the Mayer[43] and Martí-Gastaldo[42] laboratories and our own: first, the calculated geometry of H^+-MUV-10(Ca) indicates localization of H^+ on bridging oxos and, second, concomitant stabilization of Ti-based conduction-band potentials. Importantly, the *in situ* measurement of E_F through an optical redox indicator places the steady-state redox potential of photodoped MUV-10(Ca) below the HER electrochemical potential, providing an energetic justification for the ability of Ti-MOFs to be photodoped. It is important to note that the low activity of H^+ in this system would shift the HER to further negative potentials, meaning that the true difference between the E_F of MUV-10 and the HER is greater than 14 mV, implying that MUV-10 greatly stabilizes the e^-−H^+ pairs against recombination. These experiments involved a rare example of direct reduction of a molecular substrate by a photoexcited MOF

https://doi.org/10.1021/jacs.1c04808
J. Am. Chem. Soc. 2021, 143, 12609−12621

node, whereas charges typically transfer from the node to a cocatalyst. To the best of our knowledge, these experiments comprise the only measurements of MOF redox potentials without the use of electrodes, in a contactless, noninvasive technique. On the basis of these results, we hypothesize that bridging oxo units are generally necessary for Ti-MOFs to stabilize H^+ against the HER, as has been recently demonstrated for MIL-125.[82] We also expect that photodoped Ti-MOFs will serve as photocatalysts for transferring the e^-–H^+ pairs to molecular substrates. Previous reports on photocatalysis with Ti-MOFs employed the Ti cluster as a photosensitizer rather than as a site for reactivity, but the availability of OMSs of MUV-10(M), demonstrated here, will allow photoredox chemistry without cocatalysts.

The significant optical changes induced by nitrate salts or by heating may arise from structural disorder surrounding the MUV-10(M) nodes. These results suggest that structural disorder near MOF nodes may play an important role in determining MOF optical absorption properties in general. The introduction of nitrate salts caused the emergence of low-energy bands (Figure 9), and heating gave rise to absorption tails spanning the visible region (Figure 6). Naively, these changes could have been attributed to simple shifts in band-edge potentials rather reordering of the electronic structures. Computational results suggest that binding of alkali ions to the MUV-10(Ca) node causes a symmetry lowering that introduces midgap orbitals. The reversibility of the temperature-induced absorption tails demonstrated in Figure 5 suggests geometric distortion as well. In a recent study, variable-temperature IR data provided evidence for dynamic metal-linker bonding in MUV-10(Ca) and other common MOFs.[67] At higher temperatures, the metal–carboxylate linkages thermally populate a "loose" configuration that may involve an array of disordered geometries. The energetic degeneracy of the loose geometries could create a high density of midgap orbitals that would produce low-energy absorption, akin to Urbach tailing.[83,84] Although typically assumed to be crystalline, defects in MOFs, along with amorphous, liquid, and phase-change MOFs, have attracted intense attention recently,[63,64,85,86] and we propose that disorder near MOF nodes must be considered as well, especially to understand optical behavior.

Finally, these results demonstrate that a Tauc analysis is not always appropriate for assigning band gaps to MOFs. In systems with a low DOS, such as molecules and quantum dots, the energy of discrete transitions can be assigned from the peak maxima, often aided by finding the zero crossing point of the absorption derivative.[87] Although the majority of MOFs also exhibit low DOSs, a Tauc analysis is used in nearly all cases. A Tauc analysis assumes such a high DOS that the transitions between frontier orbitals cannot be identified, which is typical for amorphous and semiconducting materials.[88,89] Here, we found agreement between experimental and calculated band gap energies for MUV-10(Mn) through a Tauc analysis because the charge-transfer bands involving Mn overlapped with those involving the linker and Ti. A Tauc analysis was also appropriate for analyzing band gap energies for H^+-MUV-10(Ca) and other salt-treated variants because disorder at the MOF node introduced a spectrum of overlapping transitions between midgap orbitals. For all other MUV-10(M) materials, their wide band gaps and low DOSs required derivative analysis. These results suggest that interpreting the optical behavior of MOFs will require a reevaluation of the Tauc analysis and the band gap energies it has derived.

CONCLUSION

A combined experimental and computational effort indicates that the optical absorption of MUV-10(M) can be tuned by introduction of redox-inactive ions and by structural disorder. On one hand, expanding MUV-10(M) to include a family of Lewis acid ions (Sr^{2+}, Ba^{2+}, and Cd^{2+}) caused stabilization of the frontier orbital energies, in comparison to the original MUV-10(Ca). On the other hand, the binding of soluble electrolyte cations (H^+, Li^+, Na^+, K^+) to the metal–oxo cluster lowered the symmetry of the material, giving rise to midgap orbitals and absorption at longer wavelengths. Previous observations of photodoping (Ti^{3+} trapping) of Ti-MOFs can be explained by the stabilization of the Ti-based orbitals by either form of cations. *In situ* optical redox indicators provide direct evidence that the Ti^{3+}–H^+ pair remains indefinitely stable because its redox potential sits below that of the hydrogen-evolving reaction. With evidence that MUV-10(M) can support open metal sites at the photoactive Ti centers, this family of materials combines key design principles of the oxygen-evolving cluster, poising it as a well-defined platform for heterogeneous photoredox chemistry.

ASSOCIATED CONTENT

Supporting Information

The Supporting Information is available free of charge at https://pubs.acs.org/doi/10.1021/jacs.1c04808.

Syntheses, experimental details, elemental analysis, supplementary figures and tables, and VT-DRUV–vis and DFT data (PDF)

AUTHOR INFORMATION

Corresponding Authors

Christopher H. Hendon – *Department of Chemistry and Biochemistry and Material Science Institute, University of Oregon, Eugene, Oregon 97403, United States;* orcid.org/0000-0002-7132-768X; Email: chendon@uoregon.edu

Carl K. Brozek – *Department of Chemistry and Biochemistry and Material Science Institute, University of Oregon, Eugene, Oregon 97403, United States;* orcid.org/0000-0002-8014-7904; Email: cbrozek@uoregon.edu

Authors

Kevin Fabrizio – *Department of Chemistry and Biochemistry, University of Oregon, Eugene, Oregon 97403, United States;* orcid.org/0000-0001-9700-1824

Konstantinos A. Lazarou – *Department of Chemistry and Biochemistry, University of Oregon, Eugene, Oregon 97403, United States;* orcid.org/0000-0003-4917-8080

Lillian I. Payne – *Department of Chemistry and Biochemistry, University of Oregon, Eugene, Oregon 97403, United States*

Liam P. Twight – *Department of Chemistry and Biochemistry, University of Oregon, Eugene, Oregon 97403, United States*

Stephen Golledge – *CAMCOR–Center for Advanced Materials Characterization in Oregon, University of Oregon, Eugene, Oregon 97403, United States*

Complete contact information is available at: https://pubs.acs.org/10.1021/jacs.1c04808

Notes

The authors declare no competing financial interest.

■ ACKNOWLEDGMENTS

We gratefully acknowledge the University of Oregon for startup funds. This work made use of the CAMCOR facility of the Lorry I. Lokey Laboratories at the University of Oregon to perform VT-DRUV−vis experiments. This material is based upon work supported by the National Science Foundation through the Division of Materials Research under grant nos. DMR-2114430 and DMR-1956403. C.H.H. acknowledges the Research Corporation for Science Advances (Cottrell Award). We also acknowledge the continued support from the Extreme Science and Engineering Discovery Environment (XSEDE), which is supported by the National Science Foundation (ACI-1548562])and the PICS Coeus High Performance Computer, which is supported by the National Science Foundation (1624776).

■ REFERENCES

(1) Liang, Y.; Zhang, X.; MacMillan, D. W. C. Decarboxylative sp^3 C-N Coupling via Dual Copper and Photoredox Catalysis. *Nature* **2018**, *559* (7712), 83−88.

(2) Perry, I. B.; Brewer, T. F.; Sarver, P. J.; Schultz, D. M.; DiRocco, D. A.; MacMillan, D. W. C. Direct Arylation of Strong Aliphatic C−H Bonds. *Nature* **2018**, *560* (7716), 70−75.

(3) Le, C.; Chen, T. Q.; Liang, T.; Zhang, P.; MacMillan, D. W. C. A Radical Approach to the Copper Oxidative Addition Problem: Trifluoromethylation of Bromoarenes. *Science* **2018**, *360* (6392), 1010−1014.

(4) Nicewicz, D. A.; MacMillan, D. W. C. Merging Photoredox Catalysis with Organocatalysis: The Direct Asymmetric Alkylation of Aldehydes. *Science* **2008**, *322* (5898), 77−80.

(5) Linsebigler, A. L.; Lu, G.; Yates, J. T. Photocatalysis on TiO_2 Surfaces: Principles, Mechanisms, and Selected Results. *Chem. Rev.* **1995**, *95* (3), 735−758.

(6) Schneider, J.; Matsuoka, M.; Takeuchi, M.; Zhang, J.; Horiuchi, Y.; Anpo, M.; Bahnemann, D. W. Understanding TiO_2 photocatalysis: Mechanisms and Materials. *Chem. Rev.* **2014**, *114* (19), 9919−9986.

(7) Fei, H.; Cohen, S. M. A Robust, Catalytic Metal-Organic Framework with Open 2,2′-Bipyridine Sites. *Chem. Commun.* **2014**, *50* (37), 4810−4812.

(8) Burgess, S. A.; Kassie, A.; Baranowski, S. A.; Fritzsching, K. J.; Schmidt-Rohr, K.; Brown, C. M.; Wade, C. R. Improved Catalytic Activity and Stability of a Palladium Pincer Complex by Incorporation into a Metal−Organic Framework. *J. Am. Chem. Soc.* **2016**, *138* (6), 1780−1783.

(9) Fei, H.; Cohen, S. M. Metalation of a Thiocatechol-Functionalized Zr(IV)-Based Metal−Organic Framework for Selective C−H Functionalization. *J. Am. Chem. Soc.* **2015**, *137* (6), 2191−2194.

(10) Dinča, M.; Dailly, A.; Liu, Y.; Brown, C. M.; Neumann, D. A.; Long, J. R. Hydrogen Storage in a Microporous Metal-Organic Framework with Exposed Mn^{2+} coordination Sites. *J. Am. Chem. Soc.* **2006**, *128* (51), 16876−16883.

(11) Feng, X.; Song, Y.; Li, Z.; Kaufmann, M.; Pi, Y.; Chen, J. S.; Xu, Z.; Li, Z.; Wang, C.; Lin, W. Metal−Organic Framework Stabilizes a Low-Coordinate Iridium Complex for Catalytic Methane Borylation. *J. Am. Chem. Soc.* **2019**, *141* (28), 11196−11203.

(12) Brozek, C. K.; Miller, J. T.; Stoian, S. A.; Dinca, M. NO Disproportionation at a Mononuclear Site-Isolated Fe^{2+} Center in Fe^{2+}-MOF-5. *J. Am. Chem. Soc.* **2015**, *137* (23), 7495−7501.

(13) Metzger, E. D.; Brozek, C. K.; Comito, R. J.; Dincă, M. Selective Dimerization of Ethylene to 1-Butene with a Porous Catalyst. *ACS Cent. Sci.* **2016**, *2* (3), 148−153.

(14) Xiao, D. J.; Bloch, E. D.; Mason, J. A.; Queen, W. L.; Hudson, M. R.; Planas, N.; Borycz, J.; Dzubak, A. L.; Verma, P.; Lee, K.; Bonino, F.; Crocellà, V.; Yano, J.; Bordiga, S.; Truhlar, D. G.; Gagliardi, L.; Brown, C. M.; Long, J. R. Oxidation of Ethane to Ethanol by N 2 O in a Metal-Organic Framework with Coordinatively Unsaturated Iron(II) Sites. *Nat. Chem.* **2014**, *6* (7), 590−595.

(15) Comito, R. J.; Wu, Z.; Zhang, G.; Lawrence, J. A.; Korzyński, M. D.; Kehl, J. A.; Miller, J. T.; Dincă, M. Stabilized Vanadium Catalyst for Olefin Polymerization by Site Isolation in a Metal−Organic Framework. *Angew. Chem., Int. Ed.* **2018**, *57* (27), 8135−8139.

(16) Comito, R. J.; Metzger, E. D.; Wu, Z.; Zhang, G.; Hendon, C. H.; Miller, J. T.; Dincă, M. Selective Dimerization of Propylene with Ni-MFU-4*l*. *Organometallics* **2017**, *36* (9), 1681−1683.

(17) Dubey, R. J. C.; Comito, R. J.; Wu, Z.; Zhang, G.; Rieth, A. J.; Hendon, C. H.; Miller, J. T.; Dincă, M. Highly Stereoselective Heterogeneous Diene Polymerization by Co-MFU-4l: A Single-Site Catalyst Prepared by Cation Exchange. *J. Am. Chem. Soc.* **2017**, *139* (36), 12664−12669.

(18) Metzger, E. D.; Comito, R. J.; Hendon, C. H.; Dincă, M. Mechanism of Single-Site Molecule-like Catalytic Ethylene Dimerization in Ni-MFU-4l. *J. Am. Chem. Soc.* **2017**, *139* (2), 757−762.

(19) Miner, E. M.; Gul, S.; Ricke, N. D.; Pastor, E.; Yano, J.; Yachandra, V. K.; Van Voorhis, T.; Dincă, M. Mechanistic Evidence for Ligand-Centered Electrocatalytic Oxygen Reduction with the Conductive MOF Ni_3(Hexaiminotriphenylene)$_2$. *ACS Catal.* **2017**, *7* (11), 7726−7731.

(20) Johnson, B. A.; Bhunia, A.; Ott, S. Electrocatalytic Water Oxidation by a Molecular Catalyst Incorporated into a Metal-Organic Framework Thin Film. *Dalt. Trans.* **2017**, *46* (5), 1382−1388.

(21) Miner, E. M.; Wang, L.; Dincă, M. Modular O_2 Electroreduction Activity in Triphenylene-Based Metal−Organic Frameworks. *Chem. Sci.* **2018**, *9* (29), 6286−6291.

(22) Ding, Q.; Pan, Y.; Luo, Y.; Zhou, M.; Guan, Y.; Li, B.; Trivedi, M.; Kumar, A.; Liu, J. Photocatalytic and Ferric Ion Sensing Properties of a New Three-Dimensional Metal-Organic Framework Based on Cuboctahedral Secondary Building Units. *ACS Omega* **2019**, *4* (6), 10775−10783.

(23) Pratik, S. M.; Cramer, C. J. Predicted Efficient Visible-Light Driven Water Splitting and Carbon Dioxide Reduction Using Photoredox-Active UiO-NDI Metal Organic Framework. *J. Phys. Chem. C* **2019**, *123* (32), 19778−19785.

(24) Santiago-Portillo, A.; Remiro-Buenamañana, S.; Navalón, S.; García, H. Subphthalocyanine Encapsulated within MIL-101(Cr)-NH_2 as a Solar Light Photoredox Catalyst for Dehalogenation of α-Haloacetophenones. *Dalt. Trans.* **2019**, *48* (48), 17735−17740.

(25) Zhu, Y. Y.; Lan, G.; Fan, Y.; Veroneau, S. S.; Song, Y.; Micheroni, D.; Lin, W. Merging Photoredox and Organometallic Catalysts in a Metal−Organic Framework Significantly Boosts Photocatalytic Activities. *Angew. Chem., Int. Ed.* **2018**, *57* (43), 14090−14094.

(26) Shi, D.; He, C.; Qi, B.; Chen, C.; Niu, J.; Duan, C. Merging of the Photocatalysis and Copper Catalysis in Metal-Organic Frameworks for Oxidative C-C Bond Formation. *Chem. Sci.* **2015**, *6* (2), 1035−1042.

(27) Guo, F.; Wei, Y. P.; Wang, S. Q.; Zhang, X. Y.; Wang, F. M.; Sun, W. Y. Pt Nanoparticles Embedded in Flowerlike NH_2-UiO-68 for Enhanced Photocatalytic Carbon Dioxide Reduction. *J. Mater. Chem. A* **2019**, *7* (46), 26490−26495.

(28) Wang, C.; Xie, Z.; Dekrafft, K. E.; Lin, W. Doping Metal-Organic Frameworks for Water Oxidation, Carbon Dioxide Reduction, and Organic Photocatalysis. *J. Am. Chem. Soc.* **2011**, *133* (34), 13445−13454.

(29) Ji, P.; Manna, K.; Lin, Z.; Urban, A.; Greene, F. X.; Lan, G.; Lin, W. Single-Site Cobalt Catalysts at New $Zr_8(\mu_2\text{-}O)_8(\mu_2\text{-}OH)_4$ Metal-Organic Framework Nodes for Highly Active Hydrogenation of Alkenes, Imines, Carbonyls, and Heterocycles. *J. Am. Chem. Soc.* **2016**, *138* (37), 12234−12242.

(30) Ji, P.; Song, Y.; Drake, T.; Veroneau, S. S.; Lin, Z.; Pan, X.; Lin, W. Titanium(III)-Oxo Clusters in a Metal-Organic Framework Support Single-Site Co(II)-Hydride Catalysts for Arene Hydrogenation. *J. Am. Chem. Soc.* **2018**, *140* (1), 433−440.

https://doi.org/10.1021/jacs.1c04808
J. Am. Chem. Soc. 2021, 143, 12609−12621

(31) Song, Y.; Li, Z.; Zhu, Y.; Feng, X.; Chen, J. S.; Kaufmann, M.; Wang, C.; Lin, W. Titanium Hydroxide Secondary Building Units in Metal−Organic Frameworks Catalyze Hydrogen Evolution under Visible Light. *J. Am. Chem. Soc.* **2019**, *141* (31), 12219−12223.
(32) Zhang, H.; Lu, Y.; Zhang, Z. M.; Wang, E. B. A Three-Dimensional Metal-Organic Framework Based on Hexanuclear Copper Units with Unsaturated Cu(II) Centers. *Inorg. Chem. Commun.* **2012**, *17*, 9−12.
(33) Masoomi, M. Y.; Bagheri, M.; Morsali, A.; Junk, P. C. High Photodegradation Efficiency of Phenol by Mixed-Metal-Organic Frameworks. *Inorg. Chem. Front.* **2016**, *3* (7), 944−951.
(34) Shen, L.; Liang, S.; Wu, W.; Liang, R.; Wu, L. Multifunctional NH_2-Mediated Zirconium Metal-Organic Framework as an Efficient Visible-Light-Driven Photocatalyst for Selective Oxidation of Alcohols and Reduction of Aqueous Cr(VI). *Dalt. Trans.* **2013**, *42* (37), 13649−13657.
(35) Wang, D.; Huang, R.; Liu, W.; Sun, D.; Li, Z. Fe-Based MOFs for Photocatalytic CO_2 Reduction: Role of Coordination Unsaturated Sites and Dual Excitation Pathways. *ACS Catal.* **2014**, *4* (12), 4254−4260.
(36) Guesh, K.; Caiuby, C. A. D.; Mayoral, Á.; Díaz-García, M.; Díaz, I.; Sanchez-Sanchez, M. Sustainable Preparation of MIL-100(Fe) and Its Photocatalytic Behavior in the Degradation of Methyl Orange in Water. *Cryst. Growth Des.* **2017**, *17* (4), 1806−1813.
(37) Li, G.; Li, F.; Liu, J.; Fan, C. Fe-Based MOFs for Photocatalytic N_2 Reduction: Key Role of Transition Metal Iron in Nitrogen Activation. *J. Solid State Chem.* **2020**, *285*, 121245.
(38) Mason, J. A.; Darago, L. E.; Lukens, W. W.; Long, J. R. Synthesis and O_2 Reactivity of a Titanium(III) Metal-Organic Framework. *Inorg. Chem.* **2015**, *54* (20), 10096−10104.
(39) Dan-Hardi, M.; Serre, C.; Frot, T.; Rozes, L.; Maurin, G.; Sanchez, C.; Férey, G. A New Photoactive Crystalline Highly Porous Titanium(IV) Dicarboxylate. *J. Am. Chem. Soc.* **2009**, *131* (31), 10857−10859.
(40) Fu, Y.; Sun, D.; Chen, Y.; Huang, R.; Ding, Z.; Fu, X.; Li, Z. An Amine-Functionalized Titanium Metal-Organic Framework Photocatalyst with Visible-Light-Induced Activity for CO_2 Reduction. *Angew. Chem., Int. Ed.* **2012**, *51* (14), 3364−3367.
(41) Hendon, C. H.; Tiana, D.; Fontecave, M.; Sanchez, C.; D'arras, L.; Sassoye, C.; Rozes, L.; Mellot-Draznieks, C.; Walsh, A. Engineering the Optical Response of the Titanium-MIL-125 Metal−Organic Framework through Ligand Functionalization. *J. Am. Chem. Soc.* **2013**, *135* (30), 10942−10945.
(42) Padial, N. M.; Castells-Gil, J.; Almora-Barrios, N.; Romero-Angel, M.; da Silva, I.; Barawi, M.; García-Sánchez, A.; de la Peña O'Shea, V. A.; Martí-Gastaldo, C. Hydroxamate Titanium−Organic Frameworks and the Effect of Siderophore-Type Linkers over Their Photocatalytic Activity. *J. Am. Chem. Soc.* **2019**, *141* (33), 13124−13133.
(43) Saouma, C. T.; Tsou, C. C.; Richard, S.; Ameloot, R.; Vermoortele, F.; Smolders, S.; Bueken, B.; Dipasquale, A. G.; Kaminsky, W.; Valdez, C. N.; De Vos, D. E.; Mayer, J. M. Sodium-Coupled Electron Transfer Reactivity of Metal-Organic Frameworks Containing Titanium Clusters: The Importance of Cations in Redox Chemistry. *Chem. Sci.* **2019**, *10* (5), 1322−1331.
(44) Saouma, C. T.; Richard, S.; Smolders, S.; Delley, M. F.; Ameloot, R.; Vermoortele, F.; De Vos, D. E.; Mayer, J. M. Bulk-to-Surface Proton-Coupled Electron Transfer Reactivity of the Metal-Organic Framework MIL-125. *J. Am. Chem. Soc.* **2018**, *140* (47), 16184−16189.
(45) Cox, N.; Pantazis, D. A.; Neese, F.; Lubitz, W. Biological Water Oxidation. *Acc. Chem. Res.* **2013**, *46* (7), 1588−1596.
(46) Umena, Y.; Kawakami, K.; Shen, J. R.; Kamiya, N. Crystal Structure of Oxygen-Evolving Photosystem II at a Resolution of 1.9Å. *Nature* **2011**, *473* (7345), 55−60.
(47) Mukhopadhyay, S.; Mandal, S. K.; Bhaduri, S.; Armstrong, W. H. Manganese Clusters with Relevance to Photosystem II. *Chem. Rev.* **2004**, *104* (9), 3981−4026.
(48) Schuth, N.; Zaharieva, I.; Chernev, P.; Berggren, G.; Anderlund, M.; Styring, S.; Dau, H.; Haumann, M. Kα X-Ray Emission Spectroscopy on the Photosynthetic Oxygen-Evolving Complex Supports Manganese Oxidation and Water Binding in the S_3 State. *Inorg. Chem.* **2018**, *57* (16), 10424−10430.
(49) Tsui, E. Y.; Tran, R.; Yano, J.; Agapie, T. Redox-Inactive Metals Modulate the Reduction Potential in Heterometallic Manganese−Oxido Clusters. *Nat. Chem.* **2013**, *5* (4), 293−299.
(50) Tsui, E. Y.; Agapie, T. Reduction Potentials of Heterometallic Manganese-Oxido Cubane Complexes Modulated by Redox-Inactive Metals. *Proc. Natl. Acad. Sci. U. S. A.* **2013**, *110* (25), 10084−10088.
(51) Greiner, S.; Schwarz, B.; Ringenberg, M.; Dürr, M.; Ivanovic-Burmazovic, I.; Fichtner, M.; Anjass, M.; Streb, C. Redox-Inactive Ions Control the Redox-Activity of Molecular Vanadium Oxides. *Chem. Sci.* **2020**, *11* (17), 4450−4455.
(52) Kanady, J. S.; Tsui, E. Y.; Day, M. W.; Agapie, T. A Synthetic Model of the Mn3Ca Subsite of the Oxygen-Evolving Complex in Photosystem II. *Science* **2011**, *333* (6043), 733−736.
(53) Castells-Gil, J.; Padial, N. M.; Almora-Barrios, N.; Albero, J.; Ruiz-Salvador, A. R.; González-Platas, J.; García, H.; Martí-Gastaldo, C. Chemical Engineering of Photoactivity in Heterometallic Titanium−Organic Frameworks by Metal Doping. *Angew. Chem., Int. Ed.* **2018**, *57* (28), 8453−8457.
(54) Paul, A.; Borrelli, R.; Bouyanfif, H.; Gottis, S.; Sauvage, F. Tunable Redox Potential, Optical Properties, and Enhanced Stability of Modified Ferrocene-Based Complexes. *ACS Omega* **2019**, *4* (12), 14780−14789.
(55) Perdew, J. P.; Burke, K.; Ernzerhof, M. Generalized Gradient Approximation Made Simple. *Phys. Rev. Lett.* **1996**, *77* (18), 3865−3868.
(56) Kresse, G.; Furthmüller, J. Efficiency of *Ab-Initio* Total Energy Calculations for Metals and Semiconductors Using a Plane-Wave Basis Set. *Comput. Mater. Sci.* **1996**, *6* (1), 15−50.
(57) Kresse, G.; Furthmüller, J. Efficient Iterative Schemes for *Ab Initio* Total-Energy Calculations Using a Plane-Wave Basis Set. *Phys. Rev. B: Condens. Matter Mater. Phys.* **1996**, *54* (16), 11169−11186.
(58) Kresse, G.; Hafner, J. *Ab Initio* Molecular Dynamics for Liquid Metals. *Phys. Rev. B: Condens. Matter Mater. Phys.* **1993**, *47* (1), 558−561.
(59) Krukau, A. V.; Vydrov, O. A.; Izmaylov, A. F.; Scuseria, G. E. Influence of the Exchange Screening Parameter on the Performance of Screened Hybrid Functionals. *J. Chem. Phys.* **2006**, *125* (22), 224106.
(60) Butler, K. T.; Hendon, C. H.; Walsh, A. Electronic Chemical Potentials of Porous Metal−Organic Frameworks. *J. Am. Chem. Soc.* **2014**, *136* (7), 2703−2706.
(61) Padial, N. M.; Lerma-Berlanga, B.; Almora-Barrios, N.; Castells-Gil, J.; da Silva, I.; de la Mata, M.; Molina, S. I.; Hernández-Saz, J.; Platero-Prats, A. E.; Tatay, S.; Martí-Gastaldo, C. Heterometallic Titanium−Organic Frameworks by Metal-Induced Dynamic Topological Transformations. *J. Am. Chem. Soc.* **2020**, *142* (14), 6638−6648.
(62) Padial, N. M.; Lerma-Berlanga, B.; Almora-Barrios, N.; Castells-Gil, J.; da Silva, I.; de la Mata, M.ıa; Molina, S. I.; Hernandez-Saz, J.; Platero-Prats, A. E.; Tatay, S.; Martı-Gastaldo, C. Heterometallic Titanium-Organic Frameworks by Metal-Induced Dynamic Topological Transformations. *J. Am. Chem. Soc.* **2020**, *142* (14), 6638−6648.
(63) Abánades Lázaro, I.; Almora-Barrios, N.; Tatay, S.; Martí-Gastaldo, C. Effect of Modulator Connectivity in Promoting Defectivity in Titanium-Organic Frameworks. *Chem. Sci.* **2021**, *12* (7), 2586−2593.
(64) Castells-Gil, J.; Padial, N. M.; Almora-Barrios, N.; Gil-San-Millan, R.; Romero-Angel, M.; Torres, V.; da Silva, I.; Vieira, B. C.J.; Waerenborgh, J. C.; Jagiello, J.; Navarro, J. A.R.; Tatay, S.; Marti-Gastaldo, C. Heterometallic Titanium-Organic Frameworks as Dual-Metal Catalysts for Synergistic Non-Buffered Hydrolysis of Nerve Agent Simulants. *Chem.* **2020**, *6* (11), 3118−3131.
(65) Shannon, R. D. Revised Effective Ionic Radii and Systematic Studies of Interatomic Distances in Halides and Chalcogenides. *Acta*

https://doi.org/10.1021/jacs.1c04808
J. Am. Chem. Soc. 2021, 143, 12609−12621

Crystallogr., Sect. A: Cryst. Phys., Diffr., Theor. Gen. Crystallogr. **1976**, *32* (5), 751−767.
(66) Lopez-Maya, E.; Padial, N. M.; Castells-Gil, J.; Ganivet, C. R.; Rubio-Gaspar, A.; Cirujano, F. G.; Almora-Barrios, N.; Tatay, S.; Navalon, S.; Marti-Gastaldo, C. Selective Implantation of Diamines for Cooperative Catalysis in Isoreticular Heterometallic Titanium-organic Frameworks. *Angew. Chem., Int. Ed.* **2021**, *60* (21), 11868−11873.
(67) Andreeva, A. B.; Le, K. N.; Chen, L.; Kellman, M. E.; Hendon, C. H.; Brozek, C. K. Soft Mode Metal-Linker Dynamics in Carboxylate MOFs Evidenced by Variable-Temperature Infrared Spectroscopy. *J. Am. Chem. Soc.* **2020**, *142* (45), 19291−19299.
(68) Carroll, G. M.; Schimpf, A. M.; Tsui, E. Y.; Gamelin, D. R. Redox Potentials of Colloidal N-Type ZnO Nanocrystals: Effects of Confinement, Electron Density, and Fermi-Level Pinning by Aldehyde Hydrogenation. *J. Am. Chem. Soc.* **2015**, *137* (34), 11163−11169.
(69) Carroll, G. M.; Brozek, C. K.; Hartstein, K. H.; Tsui, E. Y.; Gamelin, D. R. Potentiometric Measurements of Semiconductor Nanocrystal Redox Potentials. *J. Am. Chem. Soc.* **2016**, *138* (13), 4310−4313.
(70) Carroll, G. M.; Tsui, E. Y.; Brozek, C. K.; Gamelin, D. R. Spectroelectrochemical Measurement of Surface Electrostatic Contributions to Colloidal CdSe Nanocrystal Redox Potentials. *Chem. Mater.* **2016**, *28* (21), 7912−7918.
(71) Connelly, N. G.; Geiger, W. E. Chemical Redox Agents for Organometallic Chemistry. *Chem. Rev.* **1996**, *96* (2), 877−910.
(72) Pavlishchuk, V. V.; Addison, A. W. Conversion Constants for Redox Potentials Measured versus Different Reference Electrodes in Acetonitrile Solutions at 25°C. *Inorg. Chim. Acta* **2000**, *298* (1), 97−102.
(73) Morimoto, Y.; Kotani, H.; Park, J.; Lee, Y. M.; Nam, W.; Fukuzumi, S. Metal Ion-Coupled Electron Transfer of a Nonheme Oxoiron(IV) Complex: Remarkable Enhancement of Electron-Transfer Rates by Sc^{3+}. *J. Am. Chem. Soc.* **2011**, *133* (3), 403−405.
(74) Fukuzumi, S.; Morimoto, Y.; Kotani, H.; Naumov, P.; Lee, Y.-M.; Nam, W. Crystal Structure of a Metal Ion-Bound Oxoiron(IV) Complex and Implications for Biological Electron Transfer. *Nat. Chem.* **2010**, *2* (9), 756−759.
(75) Brozek, C. K.; Hartstein, K. H.; Gamelin, D. R. Potentiometric Titrations for Measuring the Capacitance of Colloidal Photodoped ZnO Nanocrystals. *J. Am. Chem. Soc.* **2016**, *138* (33), 10605−10610.
(76) Brozek, C. K.; Zhou, D.; Liu, H.; Li, X.; Kittilstved, K. R.; Gamelin, D. R. Soluble Supercapacitors: Large and Reversible Charge Storage in Colloidal Iron-Doped ZnO Nanocrystals. *Nano Lett.* **2018**, *18* (5), 3297−3302.
(77) Schimpf, A. M.; Ochsenbein, S. T.; Buonsanti, R.; Milliron, D. J.; Gamelin, D. R. Comparison of Extra Electrons in Colloidal N-Type Al^{3+}-Doped and Photochemically Reduced ZnO Nanocrystals. *Chem. Commun.* **2012**, *48* (75), 9352.
(78) Schimpf, A. M.; Knowles, K. E.; Carroll, G. M.; Gamelin, D. R. Electronic Doping and Redox-Potential Tuning in Colloidal Semiconductor Nanocrystals. *Acc. Chem. Res.* **2015**, *48* (7), 1929−1937.
(79) Boettcher, S. W.; Oener, S. Z.; Lonergan, M. C.; Surendranath, Y.; Ardo, S.; Brozek, C.; Kempler, P. A. Potentially Confusing: Potentials in Electrochemistry. *ACS Energy Lett.* **2021**, *6* (1), 261−266.
(80) Liu, H.; Brozek, C. K.; Sun, S.; Lingerfelt, D. B.; Gamelin, D. R.; Li, X. A Hybrid Quantum-Classical Model of Electrostatics in Multiply Charged Quantum Dots. *J. Phys. Chem. C* **2017**, *121* (46), 26086−26095.
(81) Hartstein, K. H.; Brozek, C. K.; Hinterding, S. O. M.; Gamelin, D. R. Copper-Coupled Electron Transfer in Colloidal Plasmonic Copper-Sulfide Nanocrystals Probed by in Situ Spectroelectrochemistry. *J. Am. Chem. Soc.* **2018**, *140* (9), 3434−3442.
(82) Mancuso, J. L.; Fabrizio, K.; Brozek, C. K.; Hendon, C. H. On the limit of proton-coupled electronic doping in a Ti(IV)-containing MOF. *Chem. Sci.* **2021**, DOI: 10.1039/D1SC03019A.
(83) John, S.; Soukoulis, C.; Cohen, M. H.; Economou, E. N. Theory of Electron Band Tails and the Urbach Optical-Absorption Edge. *Phys. Rev. Lett.* **1986**, *57* (14), 1777−1780.
(84) Ikhmayies, S. J.; Ahmad-Bitar, R. N. A Study of the Optical Bandgap Energy and Urbach Tail of Spray-Deposited CdS:In Thin Films. *J. Mater. Res. Technol.* **2013**, *2* (3), 221−227.
(85) Lee, S.; Bürgi, H.-B.; Alshmimri, S. A.; Yaghi, O. M. Impact of Disordered Guest−Framework Interactions on the Crystallography of Metal−Organic Frameworks. *J. Am. Chem. Soc.* **2018**, *140* (28), 8958−8964.
(86) Cheetham, A. K.; Bennett, T. D.; Coudert, F.-X.; Goodwin, A. L. Defects and Disorder in Metal Organic Frameworks. *Dalt. Trans.* **2016**, *45* (10), 4113−4126.
(87) Zanatta, A. R. Revisiting the Optical Bandgap of Semiconductors and the Proposal of a Unified Methodology to Its Determination. *Sci. Rep.* **2019**, *9* (1), 11225.
(88) Dolgonos, A.; Mason, T. O.; Poeppelmeier, K. R. Direct Optical Band Gap Measurement in Polycrystalline Semiconductors: A Critical Look at the Tauc Method. *J. Solid State Chem.* **2016**, *240*, 43−48.
(89) Tauc, J. Optical Properties and Electronic Structure of Amorphous Ge and Si. *Mater. Res. Bull.* **1968**, *3* (1), 37−46.